Title	Design and analysis of magnet proportioning for dual-memory machines
Author(s)	Li, F; Chau, KT; Liu, C; Jiang, J; Wang, WY
Citation	IEEE Transactions on Applied Superconductivity, 2012, v. 22 n. 3, p. 4905404:1-4
Issued Date	2012
URL	http://hdl.handle.net/10722/164044
Rights	Creative Commons: Attribution 3.0 Hong Kong License

Design and Analysis of Magnet Proportioning for Dual-Memory Machines

Fuhua Li, K. T. Chau, *Senior Member, IEEE*, Chunhua Liu, *Member, IEEE*, J. Z. Jiang, and Winson Yong Wang

***Abstract*—The dual-memory machine utilizes two kinds of permanent magnets (PMs), namely the aluminum-nickel-cobalt (Al-Ni-Co) and neodymium-iron-boron (Nd-Fe-B) materials, to provide effective flux-mnemonic feature. Namely, the Al-Ni-Co PM can be forward or backward magnetized in such a way that it can coordinate with the Nd-Fe-B PM to online tune the air-gap flux density. Based on the proposed DC-excited memory machine structure, the magnet proportioning between the Al-Ni-Co PM and the Nd-Fe-B PM is analysed. Both simulation and experimentation are carried out to verify the validity of the proposed dual-memory machine design.**

***Index Terms*—Dual-memory, flux-mnemonic machine, magnet proportioning, memory machine, permanent magnet machine.**

I. Introduction

THE MEMORY machine is a kind of PM brushless machines [1], [2] having the flux-mnemonic feature. Initially, the memory machine was based on the PM synchronous machine structure in which the Al-Ni-Co PM is located in the rotor and online magnetized or demagnetized by the d-axis stator armature current field [3], [4], thus termed as the AC-excited memory machine. Recently, the DC-excited memory machine has been developed in which both the Al-Ni-Co PM and the armature winding are located in the stator while the online magnetization or demagnetization is by a magnetizing winding also located in the stator [5], [6]. Notice that this magnetizing winding is much smaller than the field winding adopted by PM hybrid machines [7]. However, these memory machines still suffer from two drawbacks—the Al-Ni-Co PM has a much lower energy product than the Nd-Fe-B PM; and the Al-Ni-Co PM is prone to be accidentally demagnetized.

By adopting two kinds of PM materials, namely the Al-Ni-Co and Nd-Fe-B, they can complement one another to solve the aforementioned drawbacks. Rather than based on the AC-excited memory machine structure [8], the dual-memory concept is incorporated into the DC-excited memory machine. Hence, this dual-memory machine not only inherits the merits of flux-mnemonic and straightforward magnetization, but also solves the drawbacks of relatively low PM energy product and accidental PM demagnetization. This machine is particularly useful for those applications desiring a wide range of air-gap flux density such as the motor for electric vehicles or the generator for wind turbines.

Manuscript received September 13, 2011; accepted December 04, 2011. Date of publication December 21, 2011; date of current version May 24, 2012. This work was supported by a grant (Project HKU710710E) from the Hong Kong Research Grants Council, Hong Kong Special Administrative Region, China.

F. Li, K. T. Chau, C. Liu, and J. Z. Jiang are with The University of Hong Kong, Hong Kong, China (e-mail: fhli@eee.hku.hk).

W. Y. Wang is with Johnson Electric, Hong Kong, China.

Color versions of one or more of the figures in this paper are available online at http://ieeexplore.ieee.org.

Digital Object Identifier 10.1109/TASC.2011.2180494

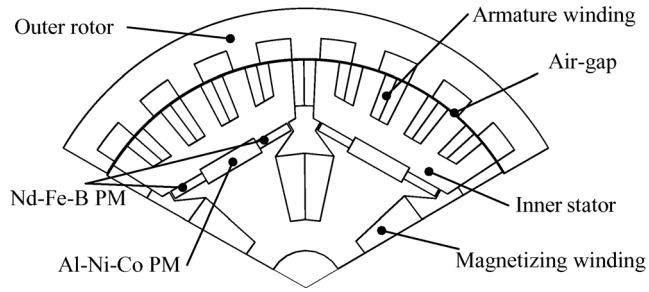

Fig. 1. Machine structure.

The purpose of this paper is to propose the design of magnet proportioning between the Al-Ni-Co PM and the Nd-Fe-B PM for the dual-memory machines in such a way the optimal flux control range can be achieved. Equivalent magnetic circuits will be formulated for this analysis. Both simulation and experimentation will be given to verify the proposed design.

II. Machine Design

Fig. 1 shows the proposed machine structure. This machine adopts the 5-phase, outer-rotor and double-layer inner-stator configuration. The outer rotor is made of simple iron core with salient poles that can provide high robustness. The double-layer inner stator accommodates the armature winding in the upper layer and the PM in the lower layer. This arrangement can reduce the possibility of accidental demagnetization of the Al-Ni-Co PM by the armature field. Three PM pieces, including two Nd-Fe-B PM pieces and one Al-Ni-Co PM piece, constitute a PM pole in the stator. The magnetizing winding is located in the inner space of the stator, which functions to online magnetize the Al-Ni-Co PM in forward or backward direction. The Al-Ni-Co PM provides a tunable PM flux while the Nd-Fe-B PM provides a constant PM flux, hence achieving strong and adjustable air-gap flux density.

Fig. 2 depicts the simplified magnetic flux diagram. It can be seen that the flux linking through two neighboring Nd-Fe-B PM pieces is within one closed flux loop, whereas the flux passing through the Al-Ni-Co PM piece belongs to two closed flux loops.

III. Magnetic Circuits for Magnet Proportioning

The proposed dual-memory machine incorporates two kinds of PMs to provide the magnetomotive force (MMF). The Al-Ni-Co PM can be forward or backward magnetized by the magnetizing winding. When the machine works under normal operation, the Al-Ni-Co PM is fully forward magnetized in the same magnetization direction as the neighboring Nd-Fe-B PM so that the maximum air-gap flux density can be achieved.

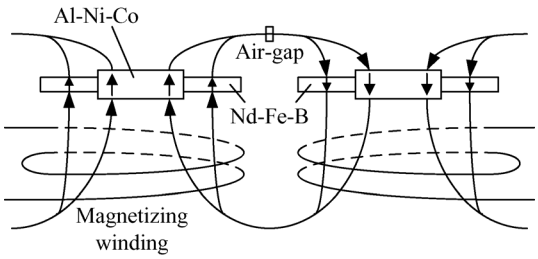

Fig. 2. Simplified magnetic flux diagram.

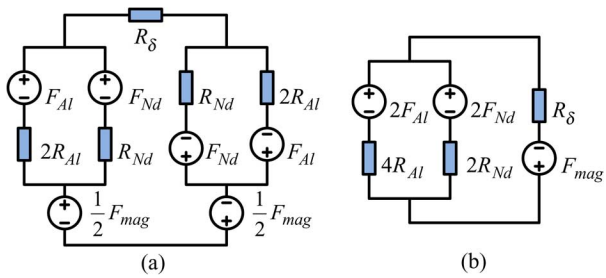

Fig. 3. Equivalent magnetic circuits under forward magnetization. (a) Original. (b) Simplified.

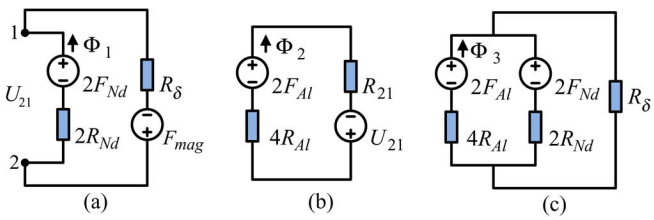

Fig. 4. Magnetic circuit analysis under forward magnetization. (a) Thevenin equivalent MMF and reluctance. (b) Thevenin equivalent magnetic circuit. (c) Equivalent magnetic circuit under no magnetizing MMF.

Under the light-load or high-speed condition, the Al-Ni-Co PM is backward magnetized so as to weaken the flux produced by the Nd-Fe-B PM, hence achieving flux-weakening operation.

A. Forward Magnetization Analysis

The equivalent magnetic circuits describing the forward magnetization, also called flux-enhancing, are depicted in Fig. 3 where F_{mag} is the magnetizing winding MMF, F_{Al} is the Al-Ni-Co PM MMF, R_{Al} is the Al-Ni-Co PM reluctance, F_{Nd} is the Nd-Fe-B PM MMF, R_{Nd} is the Nd-Fe-B PM reluctance and R_δ is the air-gap reluctance. Since the magnetic circuit shown in Fig. 3(a) is symmetrical, it can be further simplified as Fig. 3(b). The magnetic circuit analysis is carried out as detailed in Fig. 4 where Φ_1 is the flux passing through the Nd-Fe-B PM, Φ_2 is the flux passing through the Al-Ni-Co PM, U_{21} is the Thevenin equivalent MMF and R_{21} is the Thevenin equivalent reluctance.

Firstly, the Al-Ni-Co PM is omitted as shown in Fig. 4(a). The magnetic flux passing through the Nd-Fe-B PM is expressed as:

$$\Phi_1 = \frac{2F_{Nd} + F_{mag}}{2R_{Nd} + R_\delta} \tag{1}$$

Thus, the Thevenin equivalent MMF and reluctance can be calculated as given by:

$$U_{21} = F_{mag} - R_\delta \Phi_1 = \frac{2F_{mag}R_{Nd}}{2R_{Nd} + R_\delta} - \frac{2F_{Nd}R_\delta}{2R_{Nd} + R_\delta} \tag{2}$$

$$R_{21} = \frac{2R_{Nd}R_\delta}{2R_{Nd} + R_\delta} \tag{3}$$

Secondly, as shown in Fig. 4(b), the use of Thevenin equivalent MMF and reluctance can further simplify the magnetic circuit. Actually, the Thevenin equivalent MMF serves to magnetize the Al-Ni-Co PM. Since the second term of (2) is governed by the Nd-Fe-B PM MMF, the magnetizing MMF should be large enough to compensate this Nd-Fe-B PM MMF in order to forward magnetize the Al-Ni-Co PM. From (2), the criterion for forward magnetization of the Al-Ni-Co PM can be derived as:

$$\frac{2F_{mag}R_{Nd}}{2R_{Nd} + R_\delta} - \frac{2F_{Nd}R_\delta}{2R_{Nd} + R_\delta} \geq 3H_{Al}2h_{Al} \tag{4}$$

where H_{Al} and h_{Al} are the coercivity and thickness of the Al-Ni-Co PM, respectively.

Thirdly, if the magnetizing winding is out of service, as shown in Fig. 4(c), the Thevenin equivalent MMF will only be dependent on the Nd-Fe-B PM MMF as given by:

$$U_{21} = U_{ms} = -\frac{2F_{Nd}R_\delta}{2R_{Nd} + R_\delta} \tag{5}$$

The negative sign in (5) indicates that the Nd-Fe-B PM tends to reversely magnetize the Al-Ni-Co PM. Thus, it is necessary to ensure that the Al-Ni-Co PM is thick enough to withstand this field strength. Also, for the sake of high air-gap flux density, the flux passing through the Al-Ni-Co PM should be as large as possible. Therefore, the criterion for selection of the Al-Ni-Co PM thickness can be deduced from (5) as:

$$\frac{2F_{Nd}R_\delta}{2R_{Nd} + R_\delta} \leq 0.5H_{Al}2h_{Al} \tag{6}$$

Hence, it yields:

$$h_{Al} \geq \frac{2F_{Nd}R_\delta}{H_{Al}(2R_{Nd} + R_\delta)} \tag{7}$$

Fig. 5 depicts the forward and backward magnetization processes of the Al-Ni-Co PM. For the case of forward magnetization as illustrated in Fig. 5(a), the Al-Ni-Co PM is initially not magnetized, namely operating at the origin O. When the Al-Ni-Co PM and the Nd-Fe-B PM coexist, the Al-Ni-Co PM is reversely magnetized by the Nd-Fe-B PM so that the operating point moves to P_1. Then, when the magnetizing winding is excited, the Al-Ni-Co PM becomes forward magnetized, thus moving to the operating point P_2. Consequently, after removing the excitation of the magnetizing winding, the operating point moves to P_3.

B. Backward Magnetization Analysis

The backward magnetization, also called flux-weakening, is to reversely magnetize the Al-Ni-Co PM, which serves to weaken or cancel the magnetic field produced by the Nd-Fe-B PM. The corresponding magnetic circuit analysis is illustrated in Fig. 6.

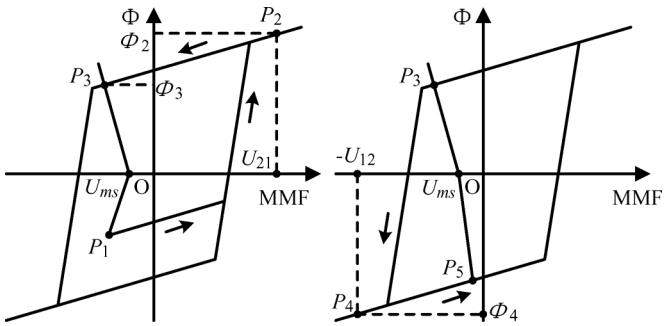

Fig. 5. Magnetization processes of Al-Ni-Co PM. (a) Forward magnetization. (b) Backward magnetization.

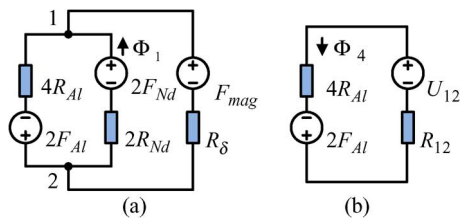

Fig. 6. Magnetic circuit analysis under backward magnetization. (a) Equivalent magnetic circuit. (b) Thevenin equivalent magnetic circuit.

Similar to the previous derivation for forward magnetization, the Al-Ni-Co PM is first omitted to derive the Thevenin equivalent magnetic circuit. Based on Fig. 6(a), the Thevenin equivalent MMF and reluctance can be calculated as given by:

$$U_{12} = \frac{2F_{Nd}R_\delta}{2R_{Nd}+R_\delta} + \frac{F_{mag}2R_{Nd}}{2R_{Nd}+R_\delta} \tag{8}$$

$$R_{12} = R_{21} \tag{9}$$

Hence, as shown in Fig. 6(b), the use of Thevenin equivalent MMF and reluctance can further simplify the magnetic circuit. Since the Thevenin equivalent MMF consists of two positive terms, the Nd-Fe-B PM MMF exerts a magnetizing force to assist the magnetizing winding to magnetize the Al-Ni-Co PM in the reverse direction. Thus, the required magnetizing MMF for backward magnetization is much lower than that for forward magnetization. From (8), the criterion for backward magnetization of the Al-Ni-Co can be deduced as:

$$F_{mag} \geq 3H_{Al}h_{Al}\left(2+\frac{R_\delta}{R_{Nd}}\right) - F_{Nd}\frac{R_\delta}{R_{Nd}} \tag{10}$$

Hence, the thickness of the Al-Ni-Co PMs is governed by:

$$h_{Al} \leq \frac{F_{Nd}R_\delta + F_{mag}R_{Nd}}{3H_{Al}(2R_{Nd}+R_\delta)} \tag{11}$$

The process of backward magnetization is illustrated in Fig. 5(b). Assuming that the original operating point is at P_3, it moves to P_4 when the magnetizing MMF is applied. After removing the excitation of the magnetizing winding, the operating point moves along the hysteresis loop to P_5.

It should be noted that the magnetization of the Al-Ni-Co PM may adopt various strategies to control the air-gap flux density. For examples, it can adopt forward magnetization to reinforce the Nd-Fe-B PM field, hence strengthening the air-gap flux density; it can be demagnetized so that the air-gap flux density depends only on the Nd-Fe-B PM field; or it can adopt backward magnetization to cancel out the Nd-Fe-B PM field, leading to operate as a reluctance machine.

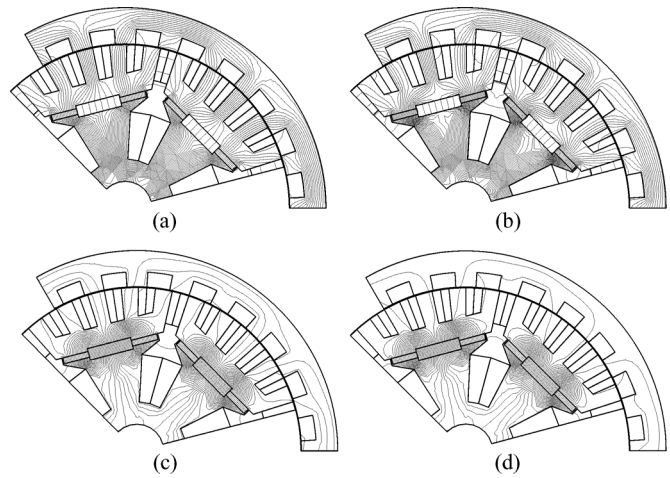

Fig. 7. Magnetic field distributions under different magnetizing currents. (a) 15 A. (b) 5 A. (c) −5 A. (d) −15 A.

IV. Simulation Results

Based on the derived equations, the dimensions of the two kinds of PMs are determined, namely $30\ \mathrm{mm} \times 8\ \mathrm{mm} \times 80\ \mathrm{mm}$ $(\mathrm{width} \times \mathrm{thickness} \times \mathrm{length})$ for the Al-Ni-Co PM and $17.4\ \mathrm{mm} \times 4\ \mathrm{mm} \times 80\ \mathrm{mm}$ for the Nd-Fe-B PM. Notice that the thickness of the Al-Ni-Co PM is twice that of the Nd-Fe-B PM. The magnetizing winding is set to be 200 turns. Consequently, the time-stepping finite element method (TS-FEM) is employed to simulate the online magnetization. Fig. 7 shows the magnetic field distributions under different magnetizing currents at the speed of 600 rpm. It can be observed that all three PM pieces (two Nd-Fe-B and one Al-Ni-Co) under the same pole provide the flux passing through the air-gap when the Al-Ni-Co is forward magnetized by 15 A, whereas the Al-Ni-Co PM piece is reversely magnetized by its neighboring Nd-Fe-B PM pieces and cannot contribute to the air-gap flux when the forward magnetizing current is reduced to 5 A. On the other side, when the Al-Ni-Co PM piece is reversely magnetized by −15 A or −5 A, the air-gap flux is significantly reduced. It should be noted that the difference between the cases of −15 A and −5 A is not so significant, which is actually due to the MMF bias provided by the Nd-Fe-B PM.

The air-gap flux density distributions under different magnetizing currents are plotted together in Fig. 8. Under forward magnetization, the air-gap flux density significantly increases with the magnetizing current increasing from 2 A to 15 A. In contrast, under backward magnetization, the changes are less significant, which is also due to the MMF bias provided by the Nd-Fe-B PM.

V. Experimental Results

The proposed dual-memory machine is prototyped for experimentation. The Al-Ni-Co 5DG PM material and the Nd-Fe-B N38SH PM material are adopted. The whole test-bed is shown in Fig. 9 in which the dual-memory machine is mechanically

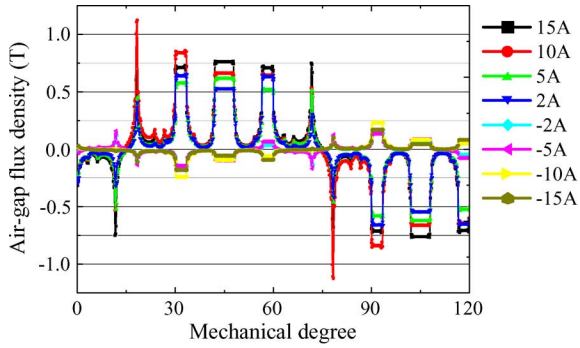

Fig. 8. Air-gap flux density distributions under different magnetizing currents.

Fig. 9. Proposed dual-memory machine prototype and test-bed.

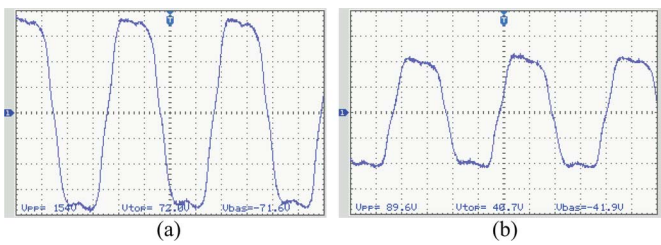

Fig. 10. Measured EMF waveforms at 600 rpm. (a) Forward magnetization (20 V/div, 1 ms/div). (b) Backward magnetization (20 V/div, 1 ms/div).

coupled with a DC dynamometer via a dynamic torque transducer. The control system is based on a DSpace controller which generates proper gating signals to drive the inverter feeding the machine.

When the proposed machine operates as a generator at 600 rpm, the no-load electromotive force (EMF) waveforms are measured under different magnetizing currents. As shown in Fig. 10, the generated EMF can achieve peak-to-peak 154 V under forward magnetization using 10 A, whereas it can be reduced to 89.6 V under backward magnetization using −5 A. Hence, the effect of forward and backward magnetizations is experimentally verified.

Fig. 11 shows the measured current waveforms when the machine operates as a motor to drive a load of 5 Nm with closed-loop control. All waveforms are trapezoidal which agrees with the theoretical operation of DC-excited memory machines [5]. Comparing the cases of forward magnetization using +10 A and backward magnetization using −10 A under the same DC-link voltage of 40 V, as shown in Figs. 11(a) and 11(c) respectively, the motor speed under forward magnetization is 160 rpm which is much faster than 90 rpm under backward magnetization. It is

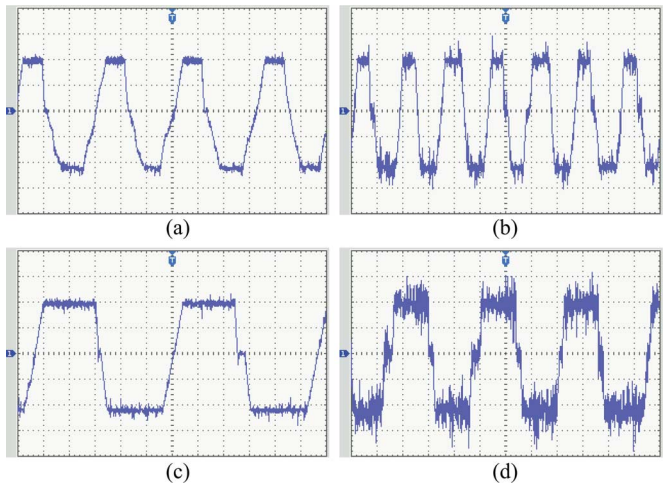

Fig. 11. Measured current waveforms at different speeds under different DC-link voltages and magnetizing currents (1.5 A/div, 5 ms/div). (a) 160 rpm, 40 V, +10 A. (b) 290 rpm, 100 V, +10 A. (c) 90 rpm, 40 V, −10 A. (d) 150 rpm, 140 V, −10 A.

expected because the air-gap flux, the driving torque and hence the motor speed are diminished when forward magnetization is changed to backward magnetization. Similar results can be observed from Figs. 11(b) and 11(d). Moreover, when comparing between Figs. 11(c) and 11(d), the motor speed can be increased from 90 rpm to 150 rpm by increasing the DC-link voltage from 40 V to 140 V. However, as shown in Fig. 11(d), the high voltage creates more current ripples which are undesirable.

VI. Conclusion

This paper has proposed and implemented the dual-memory machine. It incorporates both the Al-Ni-Co PM and Nd-Fe-B PM materials. The magnet proportioning criteria are analytically derived which are essential for the design of this machine. Two key machine operations, namely the forward magnetization and backward magnetization, are verified by using the TS-FEM. Finally, the experimental results further verify the validity of the proposed machine.

References

[1] K. T. Chau, C. C. Chau, and C. Liu, "Overview of permanent magnet brushless drives for electric and hybrid electric vehicles," *IEEE Trans. Industrial Electronics*, vol. 55, no. 6, pp. 2246–2257, 2008.

[2] C. Liu, K. T. Chau, and J. Z. Jiang, "A permanent-magnet hybrid brushless integrated-starter-generator for hybrid electric vehicles," *IEEE Trans. Industrial Electronics*, vol. 57, no. 12, pp. 4055–4064, 2010.

[3] V. Ostovic, "Memory motors," *IEEE Industry Applications Magazine*, vol. 9, no. 1, pp. 52–61, 2003.

[4] J. H. Lee and J. P. Hong, "Permanent magnet demagnetization characteristic analysis of a variable flux memory motor using coupled Preisach modeling and FEM," *IEEE Trans. Magnetics*, vol. 44, no. 6, pp. 1550–1553, 2008.

[5] C. Yu and K. T. Chau, "Design, analysis, and control of DC-excited memory motors," *IEEE Trans. Energy Conversion*, vol. 26, no. 2, pp. 479–489, 2011.

[6] C. Yu and K. T. Chau, "Dual-mode operation of DC-excited memory motors under flux regulation," *IEEE Trans. Industry Applications*, vol. 47, no. 5, pp. 2031–2041, 2011.

[7] C. Liu, K. T. Chau, and J. Z. Jiang, "Design of a new outer-rotor permanent-magnet hybrid machine for wind power generation," *IEEE Trans. Magnetics*, vol. 44, no. 6, pp. 1494–1497, 2008.

[8] K. Sakai, K. Yuki, Y. Hashiba, N. Takahashi, and K. Yasui, "Principle of the variable-magnetic-force memory motor," in *Int. Conf. Electr. Mach. Syst.*, 2009, pp. 1–6.